Temperature dependency of resonance fluorescence from InAs/GaAs quantum dots: Dephasing mechanisms

Joanna M. Zajac*
Institute of Photonics and Quantum Science, SUPA, Heriot-Watt University, EH14 4AS Edinburgh, United Kingdom

Sigurdur I. Erlingsson
School of Science and Engineering, Reykjavik University, Menntavegi 1, IS-101 Reykjavik, Iceland
(Received 5 March 2016; revised manuscript received 9 June 2016; published 20 July 2016)

We report a study on temperature-dependent resonant fluorescence from InAs/GaAs quantum dots. We combined spectral and temporal measurements in order to identify sources of dephasing. In the spectral domain, we observed temperature-dependent broadening of the zero-phonon line as 0.3 μeV/K, and a temperature-dependent phonon broadband. Time-resolved autocorrelation measurements revealed temperature-dependent spin pumping times between $T_{1,s} = 6$ ns (4 K) and 0.5 ns (15 K). These results are compared against theoretical modeling with a master equation for a four-level system coupled to phonon and spin baths. We explained the results by phonon-mediated hole-spin scattering between two excited states, with the piezophonons as a dominant mechanism.

DOI: 10.1103/PhysRevB.94.035432

I. INTRODUCTION

Resonance fluorescence (RF) from semiconductor quantum dots (QDs) is a promising tool for quantum information technologies [1]. It allows for the generation of single and highly indistinguishable flying photonic qubits [2], and their manipulation and storage in QDs [3,4]. In RF, a photon stream consists of an elastic and inelastic fraction of scattered photons. The properties of the elastic fraction are imposed by the excitation laser [5]. The properties of the inelastic fraction are determined by environmentally induced dephasing. The figure of merit describing dephasing is a photon coherence time $T_2 = (1/2T_1 + 1/T_2^*)^{-1}$, where T_1 is a lifetime and T_2^* is a dephasing time. Dephasing resulting from the coupling between QD and its environment often limits the coherence times below the Fourier limit, where $T_2 = 2T_1$. It originates from spin [6] and charge [7] noise, and interactions with phonons [8]. Spin noise originates from a hyperfine interaction (HFI) between a localized carrier and 10^5 nuclear spins within the QD [9]. For electrons, the HFI is of contact type, and can be suppressed in external magnetic fields above 0.3 T [10]. For holes, the HFI is of dipole-dipole type, and thus significantly smaller [11]. Consequently, the dominating spin-dephasing mechanisms are phonons [12], anisotropic hyperfine interactions [13], and exchange interactions [14]. Phonons cause a dephasing of an excited state due to deformation potential coupling [8]. Until now, temperature-dependent studies on resonance fluorescence from QDs were performed in a high excitation power regime that is necessary for optical manipulation [3,15,16]. Therein, strong phonon quenching of the Rabi oscillation was reported. A phonon broadband was mapped for a QD-microcavity system [17,18] where phonon-mediated QD excitation was observed and successfully described by the polaron master equation (ME) formalism [19,20]. Here, we study temperature-dependent RF from a negative trion X^- complex in an n-doped InGa/GaAs QD sample with a particular focus on low-power excitation relevant for single photon generation.

This paper is organized in the following manner. First, we discuss the sample and experimental techniques, then we show the results of high-resolution spectral imaging on a zero-phonon line (ZPL), spectral imaging of the phonon broadband, and time-resolved autocorrelation measurements. Next, we compare data against numerical calculations. Finally, we discuss the origin of the spin pumping and conclude the paper.

II. SAMPLES

The sample studied here is a molecular beam epitaxial (MBE) grown InAs/GaAs QD structure embedded into an n-doped Schottky diode in order to achieve deterministic charge tuning [21]. It has a 25 nm tunneling barrier between the QD layer and the back contact. In order to increase the photon extraction efficiency, QDs are embedded into a thin membrane which forms a λ cavity enclosed between a 150 nm Au mirror on the bottom side and three pairs of GaAs/AlAs distributed Bragg reflectors (DBRs) on the top side. The Au mirror has a double function as it also acts as a Schottky gate. Additionally, in order to increase the extraction efficiency from the sample, a $\phi 2$ mm glass solid immersion lens (SIL) with $n = 1.9$ (950 nm) is placed above the DBRs. The RF signal from this sample yields $\propto 1$ MHz around saturation.

III. EXPERIMENTAL TECHNIQUES

Experiments were carried out in a helium bath closed-cycle cryostat with the temperature ramped between 4 and 15 K using a heater placed beneath the sample. QDs were excited resonantly with an external-cavity diode laser from Sacher, providing a wavelength stability of better than 50 MHz and tenability between 930 and 980 nm. Photoluminescence (PL) maps were taken with a nonresonant laser diode at 830 nm.

*Present address: School of Physics and Astronomy, SUPA, University of St. Andrews, North Haugh, KY16 9SS St. Andrews, United Kingdom; joanna.m.zajac@gmail.com

Resonance fluorescence (RF) was measured using a dark-field confocal microscope [22] with a polarization suppression of better than 10^7 and a signal-to-noise ratio (S/N) of better than 10^3. A Fabry-Pérot fiber-based interferometer (FPI) with a free-spectral range (FSR) of 5 GHz and 200 finesse was used for high-resolution spectral imaging of the ZPL. The phonon broadband was recorded with an Acton spectrometer with 1800 l/mm grating imaged on a nitrogen-cooled CCD camera. Time-correlated data were taken with single photon avalanche photodiodes (SPAPDs) with 64/16 ps jitter. An external magnetic field, $B_{\text{ext}} = 0.6$ T, was applied in Faraday geometry. The data reported here were taken on the negative trion, which is representative for QDs in this sample.

IV. RESULTS

A. Zero-phonon line imaging

Example high-resolution FPI spectra of ZPL are shown in Fig. 1 for a Rabi frequency Ω_R below ($\Omega = 0.6\Omega_S$) and above ($\Omega = 4\Omega_S$) saturation at $T = 4$ and 15 K. The saturation curves for these data sets are shown in the inset to Fig. 1(d), together with the fits (solid lines). Fits were done using $I \propto \frac{P}{P+P_0}$, where P is the laser excitation power and P_0 is the saturation power. Saturation powers were fitted as $P_S = 5 \pm 1$ nW at $T = 4$ K, $P_S = 8 \pm 2$ nW at $T = 15$ K. They correspond to temperature-dependent saturation Rabi frequencies [23] of $\Omega_S = 0.24$ GHz at $T = 4$ K, and $\Omega_S = 0.29$ GHz at $T = 15$ K; fits to the data are shown in the inset to Fig. 1(e). FPI data for $\Omega = 0.6\Omega_S$ and $4\Omega_S$ are plotted in Figs. 1(a)–1(d), together with independent Lorentzian fits to inelastic (solid red curve) and total (solid blue curve) fractions of RF. From the Lorentzian fits to data, we extracted the full width at half maximum (FWHM) (κ) of the central peak of the Mollow triplet. The low-power limit of κ is plotted in Fig. 1(e). It was fitted iteratively using a power-dependent data series. On the same plot we show a linear fit to the data. From there, we extracted a pure dephasing rate of $\Gamma^*(T) = 0.3 \pm 0.1$ μeV/K. The Fourier-limited width at low temperature $\kappa = 0.3$ GHz is marked with a solid blue line in Fig. 1(e). It was extracted from the low-power $g^2(t)$ data as discussed in Appendix B. The elastic to total ratio of scattered photons (El/Tot) is plotted in Fig. 1(e). It was extracted from spectrally integrated Lorentzian fits to FPI data. The solid lines shown on the plot are fits to data using $\text{El/Tot} = \frac{T2}{2T_1}\frac{1}{1+P/P_0}$. The ratio decreases with temperature from 0.85 at $T = 4$ K, 0.45 at $T = 10$ K, down to 0.2 at $T = 15$ K, which indicates an increasing pure dephasing contribution to T_2. Saturation powers extracted from El/Tot are consistent with saturation curves. Finally, for data at $T = 10$ K, we noticed an increase of the El/Tot ratio at high powers, most likely due to a small laser detuning, $\delta E = 2$ μeV, which increases the elastic fraction of scattered photons.

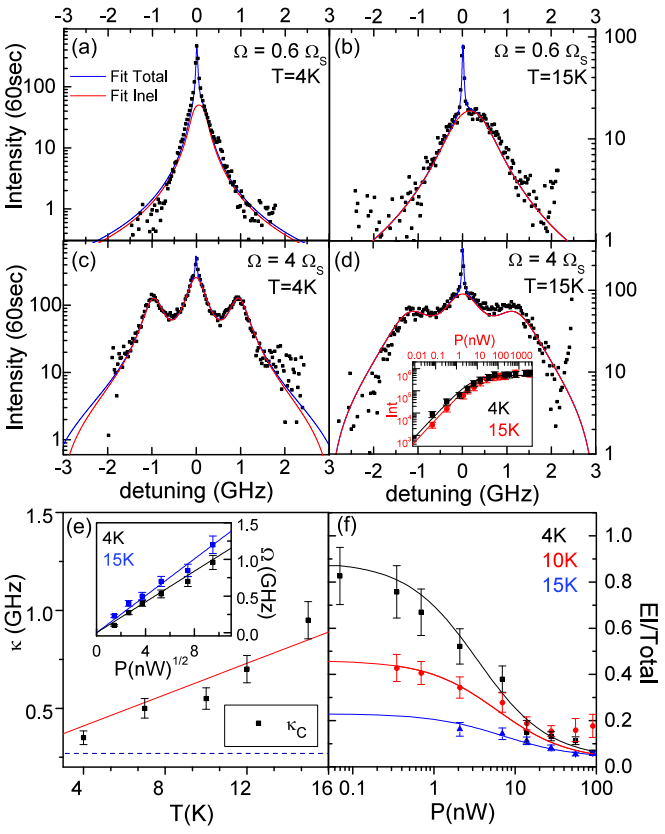

FIG. 1. In (a) and (c), high-resolution FPI spectra of ZPL at $T = 4$ K for two excitation powers below and above saturation $\Omega = 0.6\Omega_S$ and $\Omega = 4\Omega_S$, respectively. Data are plotted together with independent Lorentzian fits to inelastic (red curve) and total (blue curve) intensity. In (b) and (d), the same as (a) and (c) but at $T = 15$ K. (d) Inset: Saturation curves at $T = 4$ and 15 K, together with fits (solid lines). In (e), κ of inelastic peak for $0.6\Omega_S$ (black squares) as a function of temperature, together with fits to the data (red curve). (e) Inset: Rabi frequency (Ω_R) at $T = 4$ and 15 K as a function of temperature with linear fits. In (f), elastic to total ratio for $T = 4$, 10, and 15 K as extracted from FP data, together with fits; for more discussion, see text.

B. Phonon band imaging

The temperature-dependent spectrometer data for $\Omega \propto \Omega_S$ are shown in Fig. 2. On the side of ZPL, a phonon broadband of several meV is visible, which changes shape and intensity with temperature. The data were fitted with the polaron master equation, which adequately reproduces the temperature-dependent phonon broadband. For a discussion on the model, compare Appendix A. Parameters used for the fits [Eq. (A8)] for GaAs were: electron and hole deformation potentials $D_e = 7$ eV, and $D_h = -3.5$ eV, respectively. The longitudinal sound velocity $v_c = 4.8 \times 10^5$ cm/s; mass density $\rho = 5.3$ g/cm^3 [24]. Transition lifetime $T_1 = 0.6$ ns, and pure dephasing rate $\Gamma^* = 0.3$ μeV/K. From Eq. (A8) for $a_e \approx a_h$, phonon coupling constant leads $\alpha = \frac{(D_e - D_h)^2}{4\pi^2\rho\hbar v_c^2}$; it was extracted from the fits as $\alpha = 5 \times 10^{-8}$ GHz^{-2}. Moreover, coupling to phonons gives rise to a broadening of ZPL, which can be approximated as $\Gamma_{\text{ph}} = \pi\alpha k_B T\Omega^2$ [16], and depends on temperature and excitation power. For experimental values of $T_{\text{ph}} = 1/\Gamma_{\text{ph}}$ compare Table I. The calculated temperature-dependent Frank-Condon renormalization is $\langle B\rangle = 0.94$ at $T = 4.2$ K, $\langle B\rangle = 0.89$ at $T = 10$ K, and $\langle B\rangle = 0.84$ at $T = 15$ K. It gives rise to a temperature dependency of the Rabi frequency [16]. Here, renormalization was within 20%, as shown in the inset to Fig. 1(e), which is consistent with polaron ME calculations. We extended the model from Ref. [19] to

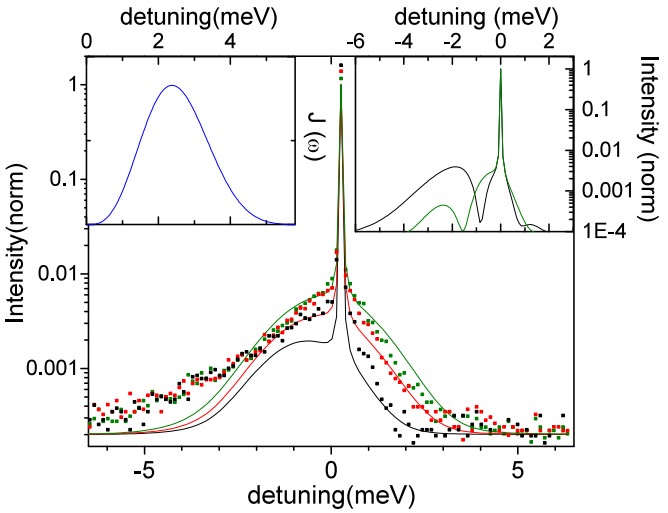

FIG. 2. Spectrometer data for $T = 4$ (black squares), 10 (red squares), and 15 K (green squares), are plotted together with corresponding fits (solid lines of the same color) at $\Omega \propto \Omega_S$. The fitting parameters are $(a_h,a_e) = (1.9,2.1)$ nm, $T_1 = 0.6$ ns, and $\Gamma^* = 0.3$ μeV/K. In the inset, the extracted phonon density of states $J(\omega)$ used for the fits in the main figure. In the right inset, a comparison between $I(\omega)$ for different electron and hole localization lengths, $(a_h,a_e) = (2,3)$ nm (green line) and $(a_h,a_e) = (1.5,4.5)$ nm (black line), revealing a double Gaussian distribution; see text for discussion.

include an explicit QD size dependency for electrons and holes; for this we modified $J(\omega)$ after Eq. (A8). $J(\omega)$ extracted from the fits is shown in the inset to Fig. 2, corresponding to localization lengths for electron and holes $(a_h,a_e) = (1.9,2.1)$nm. For distinct electron and hole localization lengths, we expect a characteristic double Gaussian distribution; compare the inset to Fig. 2, for $(a_h,a_e) = (2,3)$nm and $(a_h,a_e) = (1.5,4.5)$nm. This is not observed experimentally, and can be due to the insufficient signal-to-noise ratio of the data. This could be improved in the future by using a QD-microcavity system [17]. Finally, the content of the phonon band in RF changes from 10% ($T = 4$ K) to 26% ($T = 15$ K).

TABLE I. Values of different times constants T's. Parameters in the table were extracted from different measurements for $\Omega = \Omega_S$. $T_{s,e}$ and $T_{s,h}$ are spin pumping rates extracted from the $g^2(t)$ data set using ME fits. T^* was extracted from temperature-dependent $S(\omega)$, as outlined in Sec. IV A. T_1 was extracted from analytical fits to $g^2(t)$, as discussed in Appendix B. $T_{\rm ph}$ was extracted from ME fits to spectrometer data, as discussed in Sec. IV B. T_2 was extracted from the El/Tot ratio, as discussed in Sec. IV A. κ is a FWHM of the ZPL peak at low powers and was extracted from $S(\omega)$, as discussed in Sec. IV A.

Variable	Temperature			Data set
	4 K	10 K	15 K	
$T_{s,h}$ (ns)	6 ± 1	2 ± 0.5	0.5	$g^2(t)$
$T_{s,e}$ (ns)				
T^* (ns)	3 ± 0.2	1.4 ± 0.1	0.9 ± 0.05	FP data
T_1 (ns)		0.6 ± 0.1		$g^2(t)$
$T_{\rm ph}$ (ms)	3	1	0.7	Spectrometer
T_2 (ns)	0.9 ± 0.2	0.5 ± 0.15	0.25 ± 0.1	El/Tot
κ (GHz)	0.4	0.6	1	FP data

C. Numerical modeling of $S(\omega)$ and $g^2(t)$

In Fig. 3, we show high-resolution spectra and complimentary time-correlation data sets for two different temperatures, $T = 4$ and 15 K, and two different powers below and above saturation. Subsequently, in the spectral and time domain, we plot fits to data using a four-level master equation model. For a discussion on the model, see Appendix A. The fit parameters used here were $T_{s,h}$ and $T_{s,e}$ for hole and electron scattering times. Remaining parameters were extracted from the data, for detailed description compare caption to Table I. Fits and data show good agreement. The fits to $g^2(t)$ data were additionally convoluted with the detector response function in order to account for the finite time resolution of the system. The resolution was $\delta\tau = 64$ and 16 ps for the upper and lower data sets, respectively.

D. Spin dephasing

In the four-level master equation model discussed in Appendix A, we introduced Lindblad terms describing spin relaxation as $\Gamma_s = 1/T_{1,s}$ where $\Gamma_s = \Gamma_{s,e} + \Gamma_{s,h}$ for the electron and hole, and $\Gamma^* = 1/T^*$ for pure dephasing, in

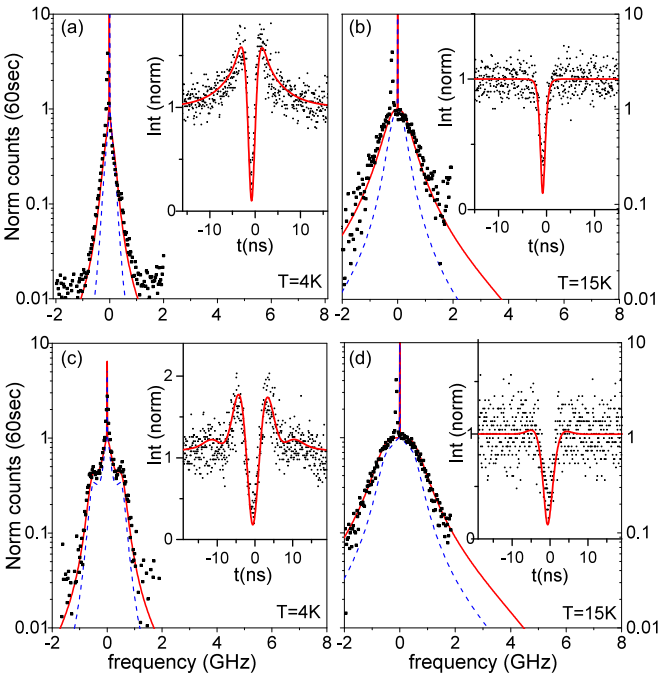

FIG. 3. High-resolution FPI spectra of the zero-phonon line (black squares) normalized to the maximum intensity of the central inelastic peak for two powers $\Omega = 0.6\Omega_S$ (upper row) and $\Omega = 2\Omega_S$ (lower row) at $T = 4$ and 15 K. Fits to data using four-level ME Eq. (A1) with (red line) and without (dashed blue line) pure dephasing. Fit parameters for (a) and (b) are listed in Table I, and for (c) and (d) the same except $T_{1,s} = 1/(7 \pm 1)$ (4 K) and $T_{1,s} = 1/(0.5 \pm 0.1)$ (15 K). In the inset, $g^2(t)$ data (black squares) with fits using the four-level ME with the same set of parameters. Time-dependent fits are convoluted with a detector response function.

order to fit the data. Below, we speculate on the physical origin of these terms. First, we will consider hole spins. The negative trion $X^{-1}|\uparrow\downarrow,\Downarrow\rangle$ is composed of two electrons in a singlet configuration $\uparrow\downarrow$, and a heavy hole $\Downarrow$. At moderate magnetic fields, two trion states, $|\uparrow\downarrow,\Downarrow\rangle$ and $|\uparrow\downarrow,\Uparrow\rangle$, are separated by hole Zeeman energy splitting. A heavy-hole–spin hyperfine contact interaction is significantly suppressed due to the p symmetry of the hole wave function. However, other scattering channels, including phonon-mediated spin relaxation, are efficient. Hole-spin relaxation rates due to the deformation potential phonons for InGaAs QDs were calculated in Ref. [12]. We extend these calculations for the temperature regime relevant for this work and adopt them for piezoelectric phonon coupling which is known to dominate for small energy transfers [25,26]. Qualitatively, the relation between the zero-temperature deformation potential scattering rate $\Gamma_{\mathrm{def},0}$ [12] and the high-temperature hole-spin relaxation due to the piezoelectric phonons is given by

$$\Gamma_{\mathrm{piezo},T} \propto \Gamma_{\mathrm{def},0} \frac{(eh_{14})^2}{\left(D_u^2 + D_u'^2\right) q_0^2} \frac{k_B T}{\delta_h}, \tag{1}$$

where eh_{14} is the piezoelectric coefficient D_u and D_u' are the deformation potential coefficients from Bir-Pikus Hamiltonian [12], q_0 is the phonon wave vector, and δ_h is the hole Zeeman splitting, for InAs. Results of the calculations are plotted in Fig. 4 as a solid blue line for $T_{\mathrm{piezo},T} = 1/\Gamma_{\mathrm{piezo},T}$; the corresponding values for the deformation potential are two orders of magnitude higher and were not plotted. Calculated values are plotted against experimental values of $T_{s,h}$ and T^*; they are in quantitative agreement. Small discrepancies between theory and experiment can be due to the uncertainty in the value of the hole g factor. In our calculations, we used $g_h = 0.55$ and $\Delta g_h = 25\%$, as discussed in Appendix A. The values of $T_{\mathrm{piezo},T}$ for $g_h \pm \Delta g_h$ were plotted as dashed blue lines.

The electron spin relaxation between $|0\rangle \leftrightarrow |1\rangle$ is denoted by $\Gamma_{s,e}$. As is known from literature [27], $\Gamma_{e,s}$ can have contributions from HF interactions, spin-orbit (SO) interactions, and tunneling with the Fermi sea of the back contact. At moderate magnetic fields $B_{\mathrm{ext}} = 0.6$ T, the contact hyperfine interaction for electrons is significantly suppressed, resulting in long spin pumping times [10]. Phonon-mediated hyperfine relaxation mechanisms [25,28], which involve scattering through orbital states, are suppressed in QD with high confinement energies [28,29]. This is the case of our sample with the 30 meV confinement potential and corresponding rates $\propto \mathrm{s}^{-1}$. Moreover, SO-induced relaxation rates are slow, and were calculated as ms^{-1} here [26]. Tunneling with the Fermi sea of a back contact contributes to the scattering rates [10,30] that for our device were estimated as $\propto \mathrm{ms}^{-1}$ at the middle of the charging plateau. However, they decrease fast when moving towards the plateau edges and are temperature dependent. $\Gamma_{s,e}$ could be related to this process. Finally, we have excluded the charge noise contribution to the experimentally observed dephasing. The effect of charge noise on RF is to increase the El/Tot ratio while pure dephasing decreases it; for details, compare Appendix C.

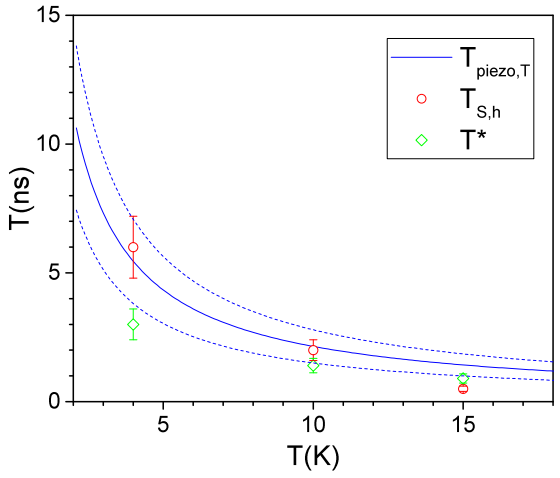

FIG. 4. Comparison between experimental, $T_{s,h}$, and theoretical, $T_{\mathrm{piezo},T}$, phonon-mediated spin relaxation times for a hole. $T_{\mathrm{piezo},T}$ are calculated after Eq. (1) and plotted as a blue solid line. Errors on $T_{\mathrm{piezo},T}$ are plotted as dashed blue lines. Compare text for more details.

V. SUMMARY

We measured RF using combined spectral and temporal detection in order to characterize dephasing. By using a high-resolution Fabry-Pérot interferometer (FPI), we characterized the temperature-dependent broadening of a zero-phonon line (ZPL), which was 0.3 μeV/K. Subsequently, employing time-resolved autocorrelation measurements, we related it to temperature-dependent spin pumping which was between 6 ns (4 K) and 0.5 ns (15 K). Furthermore, we imaged a phonon broadband resulting from the deformation potential coupling of trion to the acoustic phonon bath. These results were well reproduced by the modified polaron master equation applied to our four-level spin system. At the same time, the polaron model is not sufficient to describe broadening of ZPLs at low excitation powers. By comparing phonon-mediated spin-flip rates for electrons and holes, we explained experimental observations by the phonon-mediated spin flip of the resident hole. We subsequently excluded charge noise as a plausible source of dephasing for resonant excitation experiments. In the future, it would be interesting to measure the magnetic field dependency on the hole-spin relaxation in order to compare the contribution from piezo- and deformation phonons to the overall hole dephasing rate. In particular, they should scale with magnetic field as $\Gamma_{\mathrm{piezo}} \propto B^4$ and $\Gamma_{\mathrm{def}} \propto B^6$ in a regime where $k_B T \gg \delta_h$, where δ_h is the hole Zeeman splitting.

ACKNOWLEDGMENTS

J.M.Z. would like to acknowledge B. Gerardot for his support. J.M.Z. would also like to acknowledge E. Gauger and T. Santana for fruitful discussions on polaron modeling, as well as S. Weiler, E. Flagg, A. Nazir, and A. Muller for discussions.

J.M.Z. ran the measurements, developed the four-level PME, and performed the data fits and simulation.

S.I.E. developed and ran the simulation for the phonon-mediated hole scattering. J.M.Z. and S.I.E. both wrote the manuscript.

APPENDIX A: FOUR-LEVEL SYSTEM COUPLED TO PHONON AND SPIN RESERVOIR

We considered here a negative trion X^{-1} in the external magnetic field in Faraday geometry, compare Fig. 5 for energy level strucutre. The resulting Zeeman splitting for an electron $\delta_e = \mu_e g_e (B_{\text{ext}} + B_{z,N}) \propto 20\ \mu\text{eV}$, where g_e is an electron g factor; $\mu_e = 58\,\mu\text{eV/T}$ is the electron Bohr magneton; B_{ext} is the external magnetic field; $B_{z,N}$ is the z component of the nuclear Overhauser field. $B_{xy,N}$ give rise to a coherent coupling with $\Omega_N = g_e \mu_e B_{xy,N}/\hbar$. We excited QDs within the s shell, thus g_e is isotropic [31,32], and the g-factor tensor simplifies to $g_e = 0.55$. For a heavy-hole, g-factor tensor is anisotropic due to p symmetry of the wave function. The hole Zeeman splitting is $\delta_h = g_{h,z}\mu_e B_{\text{ext}}$ and $g_{h,z} = g_e$ [31,32]. HFI for holes is an order of magnitude smaller than for electrons, and is thus not taken into account here. Subsequently, due to the strong dependency of the g factor on QD composition and carrier localization, in calculations hereafter we used $\Delta g_{e,h} = 20\%$. In the model, we assume a laser driving $|2\rangle \rightarrow |3\rangle$ transition with Ω. The master equation takes the form

$$\frac{d\rho}{dt} = \frac{1}{i\hbar}[H,\rho] + \sum_{ij} \Gamma_{ij}\mathcal{L}[\sigma_{ij}]\rho, \tag{A1}$$

where ρ is density matrix; H is Hamiltonian; Γ_{ij} is dephasing constant; $\mathcal{L}[\sigma_{ij}]$ is Lindblad superoperator; $\sigma_{ij} = |i\rangle\langle j| = \sigma_+$ and $\sigma_{ji} = |j\rangle\langle i| = \sigma_-$ are QD transition matrices. Hamiltonian in the rotating-wave approximation is

$$H = \begin{bmatrix} -\frac{\delta_e}{2} & -\Omega_N & 0 & 0 \\ -\Omega_N & \frac{\delta_e}{2} + \Delta_{\text{ph}}^{\sigma^{ij}} & -\Omega\langle B\rangle & 0 \\ 0 & -\Omega\langle B\rangle & \Delta + \Delta_{\text{ph}}^{\sigma^{ji}} - \frac{\delta_h}{2} & 0 \\ 0 & 0 & 0 & \Delta + \frac{\delta_h}{2} \end{bmatrix}. \tag{A2}$$

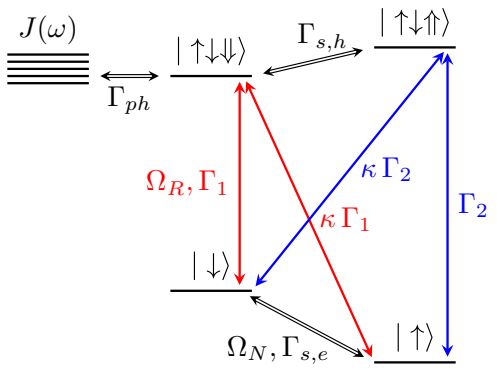

FIG. 5. Four-level system coupled to the phonon bath. We use the following notation in the text: $|\uparrow\rangle = |1\rangle$, $|\downarrow\rangle = |2\rangle$, $|\uparrow\downarrow, \Downarrow\rangle = |3\rangle$, $|\uparrow\downarrow, \Uparrow\rangle = |4\rangle$, $\Omega_R = \Omega$. Color coding reflects the transition energies: red for low-energy transitions and blue for high-energy transitions.

Lindblad terms are defined in Eq. (A4). These include the following: (i) the lifetime for the $|3\rangle \rightarrow |2\rangle$ transition $T_{23} = 1/\Gamma_{23}$, and the lifetime for the $|4\rangle \rightarrow |1\rangle$ transition $T_{14} = 1/\Gamma_{14}$, $T_{23} = T_{14} = T_1$; (ii) weak off-diagonal relaxation for $|3\rangle \rightarrow |1\rangle$ and $|4\rangle \rightarrow |2\rangle$ where $\kappa = 10^{-3}$; (iii) electron spin-flip time $T_{s,e} = 1/\Gamma_{s,e}$ between $|1\rangle \leftrightarrow |2\rangle$; (iv) hole spin-flip time $T_{s,h} = 1/\Gamma_{s,h}$ between $|3\rangle \leftrightarrow |4\rangle$; (v) phonon-mediated scattering $|2\rangle \leftrightarrow |3\rangle$ with rate $\Gamma_{\text{ph}}^{\sigma^{-/+}}$; and (vi) pure dephasing on $|2\rangle$ with Γ^*:

$$\sum_{ij}\Gamma L[\sigma_{ij}] = \sum_{12,03}^{ij}\Gamma_{ij}L[\sigma_{ij}] + \sum_{02,13}^{ij}\kappa\Gamma_{ij}L[\sigma_{ij}] + \sum_{12,21}^{ij}\Gamma_{ph}^{\sigma^{ij}}L[\sigma_{ij}] + \sum_{23,32}^{ij}\Gamma_{s,h}L[\sigma_{ij}] + \Gamma^* L[\sigma_{22}]. \tag{A3}$$

The deformation potential phonon dephasing rates after Ref. [19] are

$$\Gamma_{\text{ph}}^{\sigma^{ij,ji}} = 2\langle B\rangle^2\eta_x^2\,\text{Re}\left[\int_0^\infty d\tau e^{\pm i\Delta_{xL}\tau}(e^{\phi(\tau)} - 1)\right], \tag{A4}$$

where η_x is pump rate which is defined as $\eta_x = 2\Omega$; Δ_{xl} is laser detuning. The phonon correlation function is

$$\phi(\tau) = \int_0^\infty d\omega \frac{J(\omega)}{\omega^2}\left[\coth\frac{\beta\hbar\omega}{2}\cos(\omega\tau) - i\sin(\omega\tau)\right], \tag{A5}$$

where $\beta = \frac{1}{Tk_B}$ and T is temperature, k_B is Boltzmann constant. The thermally averaged displacement operator with phonon spectral density $J(\omega)$ is

$$\langle B\rangle = \exp\left(-\frac{1}{2}\int_0^\infty d\omega\frac{J(\omega)}{\omega^2}\coth\frac{\beta\hbar\omega}{2}\right). \tag{A6}$$

The Stark shifts are

$$\Delta_{\text{ph}}^{\sigma^{ij,ji}} = \langle B\rangle^2\eta_x^2\,\text{Im}\left[\int_0^\infty d\tau e^{\pm i\Delta_{xL}\tau}(e^{\phi(\tau)} - 1)\right]. \tag{A7}$$

The super-Ohmic phonon density of states for independent electron and hole localization lengths is

$$J(\omega) = \frac{\omega^3}{4\pi^2\rho\hbar v_c^5}\left[D_e e^{\frac{\omega^2 a_e^2}{4v_c^2}} - D_h e^{\frac{\omega^2 a_h^2}{4v_c^2}}\right]^2, \tag{A8}$$

where ρ is mass density, v_c is sound velocity in the host material, $D_{e,h}$ is electron and hole deformation potential, $a_{e,h}$ is electron and hole localization length.

In order to obtain spectra from the autocorrelation data, we used quantum regression theorem and a Fourier transform of the $g^2(t)$ data.

In Fig. 6, we illustrate the influence of different parameters on the temporary and spectrally resolved resonance fluorescence. We plot the second order-correlation function $g^2(t)$ and spectrum of emitted photons $S(\omega)$ for several values of parameters $T_{s,h}, T_{s,e}$ with fixed value of parameter T^*, as well as for varied T^* and fixed $T_{s,h}$ and $T_{s,e}$. It is apparent from the

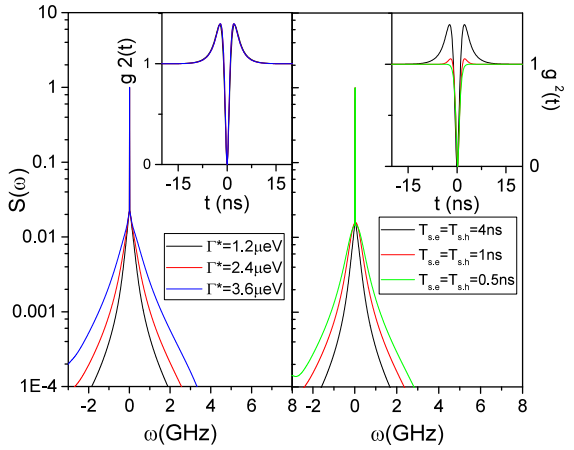

FIG. 6. Simulations illustrating the interplay between different parameters in the model. In the first column, $T_{s,h} = T_{s,e} = 4$ ns, in the second column $\Gamma^* = 1.2$ μeV; for details compare text.

simulations that both T's influence resonance fluorescence. However, the pure dephasing rate T^* does not significantly influence the $g^2(t)$ data; at the same time, it broadens $S(\omega)$. Population scattering rates $T_{s,h}, T_{s,e}$, on the other hand, influence $g^2(t)$ and $S(\omega)$. In order to reproduce the data, we had to incorporate both rates in the model.

APPENDIX B: LOW-POWER $g^2(t)$

We extracted here T_1 from low-power $g^2(t)$ data at $\Omega_R = 0.4\Omega_{RS}$ (see Fig. 7). Moreover, the data also reveal temperature-dependent spin scattering, as discussed in Appendix A. To account for these processes, we used the analytical expression, Eq. (2) in Ref. [33], extended by a spin decay term with $T_{1,s}$ as $g^{2'}(t) = g^2(t)(1 + Ae^{-\frac{t}{T_{1,s}}})$. We extracted $T_1 = 0.6$ ns, spin-flip rates $T_{1,s} = 2 \pm 1$ ns (4 K), $T_{1,s} = 1 \pm 0.5$ ns (10 K), and $T_{1,s} = 0.4 \pm 0.1$ ns (15 K).

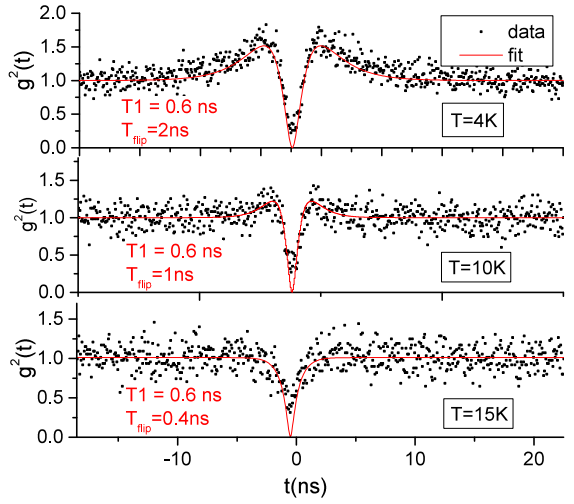

FIG. 7. Low-power $g^2(t)$ with fits.

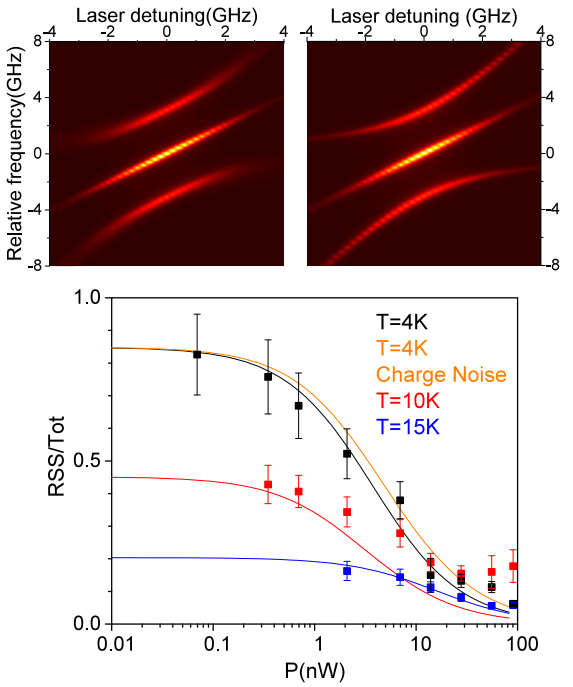

FIG. 8. Comparison between pure dephasing and charge noise effects on Mollow triplet spectra for different laser detunings. Top left: No pure dephasing but with charge noise. Top right: Pure dephasing but no charge noise. For charge noise, we used a Gaussian distribution with $\sigma = 0.7$ μeV, $T_1 = 0.6$ ns El/Tot ratios extracted from data in Sec. IV A. Bottom: Effect of charge noise and pure dephasing on El/Tot; simulations are plotted against data.

APPENDIX C: CHARGE NOISE

Charge noise was indicated as the possible cause of temperature-dependent pure dephasing [34,35]. We used here an analytical model developed in Ref. [7] to compare the effects of pure dephasing and charge noise on the broadening of the Mollow triplet and elastic to total fraction of scattered photons. We modeled our experiment with Eqs. (A2)–(A11) from Ref. [7] using a Gaussian distribution of charge noise with $\sigma = 0.7\mu$ eV as extracted from gate voltage scans of RF (not shown) with other parameters as discussed before; compare Table I. The effects of spectral diffusion and pure dephasing are illustrated in Fig. 8 and they are qualitatively different. In particular, spectral diffusion broadens the side peaks of the Mollow triplet, while pure dephasing results in a broadening of all Mollow triplets. Secondly, charge noise increases the El/Tot ratio while pure dephasing decrease it; compare Fig. 8. Experimental results, as discussed in Sec. IV A, show broadening of all Mollow triplets, an increase of the side to center peak heights, and a decrease of the elastic to total ratio; thus we concluded that charge noise cannot explain the observation from Sec. IV A.

[1] *Quantum Dots*, edited by A. Tartakovskii (Cambridge University Press, Cambridge, UK, 2012).

[2] C. Matthiesen, A. N. Vamivakas, and M. Atatüre, Phys. Rev. Lett. **108**, 093602 (2012).

[3] J. H. Quilter, A. J. Brash, F. Liu, M. Glässl, A. M. Barth, V. M. Axt, A. J. Ramsay, M. Skolnick, and A. M. Fox, Phys. Rev. Lett. **114**, 137401 (2015).

[4] W. Gao, P. Fallahi, E. Togan, A. Delteil, Y. Chin, J. Miguel-Sanchez, and A. Imamoglu, Nat. Commun. **4**, 2744 (2013).

[5] C. Matthiesen, M. Geller, C. H. H. Schulte, C. Le Gall, J. Hansom, Z. Li, M. Hugues, E. Clarke, and M. Atatüre, Nat. Commun. **4**, 1600 (2013).

[6] A. V. Kuhlmann, J. Houel, A. Ludwig, L. Greuter, D. Reuter, A. D. Wieck, M. Poggio, and R. J. Warburton, Nat. Phys. **9**, 570 (2013).

[7] K. Konthasinghe, J. Walker, M. Peiris, C. K. Shih, Y. Yu, M. F. Li, J. F. He, L. J. Wang, H. Q. Ni, Z. C. Niu, and A. Muller, Phys. Rev. B **85**, 235315 (2012).

[8] P. Borri, W. Langbein, S. Schneider, U. Woggon, R. L. Sellin, D. Ouyang, and D. Bimberg, Phys. Rev. Lett. **87**, 157401 (2001).

[9] B. Urbaszek, X. Marie, T. Amand, O. Krebs, P. Voisin, P. Maletinsky, A. Högele, and A. Imamoglu, Rev. Mod. Phys. **85**, 79 (2013).

[10] J. Dreiser, M. Atature, C. Galland, T. Muller, A. Badolato, and A. Imamoglu, Phys. Rev. B **77**, 075317 (2008).

[11] C. Testelin, F. Bernardot, B. Eble, and M. Chamarro, Phys. Rev. B **79**, 195440 (2009).

[12] L. M. Woods, T. L. Reinecke, and R. Kotlyar, Phys. Rev. B **69**, 125330 (2004).

[13] D. J. Klauser, Hyperfine interaction and spin decoherence in quantum dots, Ph.D. thesis, Universitat Basel, 2008.

[14] K. Roszak, V. M. Axt, T. Kuhn, and P. Machnikowski, Phys. Rev. B **76**, 195324 (2007).

[15] A. J. Ramsay, A. V. Gopal, E. M. Gauger, A. Nazir, B. W. Lovett, A. M. Fox, and M. S. Skolnick, Phys. Rev. Lett. **104**, 017402 (2010).

[16] Y. J. Wei, Y. He, Y. M. He, C. Y. Lu, J. W. Pan, C. Schneider, M. Kamp, S. Hofling, D. P. S. McCutcheon, and A. Nazir, Phys. Rev. Lett. **113**, 097401 (2014).

[17] S. Weiler, A. Ulhaq, S. M. Ulrich, D. Richter, M. Jetter, P. Michler, C. Roy, and S. Hughes, Phys. Rev. B **86**, 241304 (2012).

[18] A. Majumdar, E. D. Kim, Y. Gong, M. Bajcsy, and J. Vučković, Phys. Rev. B **84**, 085309 (2011).

[19] C. Roy and S. Hughes, Phys. Rev. X **1**, 021009 (2011).

[20] A. Nazir, Phys. Rev. B **78**, 153309 (2008).

[21] A. Hogele, S. Seidl, M. Kroner, K. Karrai, R. J. Warburton, B. D. Gerardot, and P. M. Petroff, Phys. Rev. Lett. **93**, 217401 (2004).

[22] A. V. Kuhlmann, J. Houel, D. Brunner, A. Ludwig, D. Reuter, A. D. Wieck, and R. J. Warburton, Rev. Sci. Instrum. **84**, 073905 (2013).

[23] M. Kroner, S. Remia, A. Hogele, S. Seidl, A. Holleitner, R. Warburton, B. Gerardot, P. Petroff, and K. Karrai, Physica E **40**, 1994 (2008).

[24] A. Vagov, V. M. Axt, T. Kuhn, W. Langbein, P. Borri, and U. Woggon, Phys. Rev. B **70**, 201305(R) (2004).

[25] S. I. Erlingsson and Y. V. Nazarov, Phys. Rev. B **66**, 155327 (2002).

[26] A. V. Khaetskii and Y. V. Nazarov, Phys. Rev. B **64**, 125316 (2001).

[27] *Spin Physics in Semiconductors*, edited by M. I. Dyakonov (Springer, Berlin, 2008).

[28] Y. G. Semenov and K. W. Kim, Phys. Rev. Lett. **92**, 026601 (2004).

[29] F. G. G. Hernandez, A. Greilich, F. Brito, M. Wiemann, D. R. Yakovlev, D. Reuter, A. D. Wieck, and M. Bayer, Phys. Rev. B **78**, 041303 (2008).

[30] J. M. Smith, P. A. Dalgarno, R. J. Warburton, A. O. Govorov, K. Karrai, B. D. Gerardot, and P. M. Petroff, Phys. Rev. Lett. **94**, 197402 (2005).

[31] A. Schwan, B. Meiners, A. Greilich, D. Yakovlev, M. Bayer, A. Maia, A. Quivy, and A. Henriques, Appl. Phys. Lett. **99**, 221914 (2011).

[32] I. A. Yugova, A. Greilich, E. A. Zhukov, D. R. Yakovlev, M. Bayer, D. Reuter, and A. D. Wieck, Phys. Rev. B **75**, 195325 (2007).

[33] E. Flagg, A. Muller, J. Robertson, S. Founta, D. Deppe, M. Xiao, W. Ma, G. Salamo, and C. K. Shih, Nat. Phys. **5**, 203 (2009).

[34] P. Borri, W. Langbein, U. Woggon, V. Stavarache, D. Reuter, and A. D. Wieck, Phys. Rev. B **71**, 115328 (2005).

[35] A. Berthelot, I. Favero, G. Cassabois, C. Voisin, C. Delalande, P. Roussignol, R. Ferreira, and J. M. Gerard, Nat. Phys. **2**, 759 (2006).